Airy-beam holographic sonogenetics for advancing neuromodulation precision and flexibility

Zhongtao Hu[a,1] (iD), Yaoheng Yang[a,1] (iD), Leqi Yang[a], Yan Gong[a] (iD), Chinwendu Chukwu[a], Dezhuang Ye[a], Yimei Yue[a], Jinyun Yuan[a], Alexxai V. Kravitz[b] (iD), and Hong Chen[a,c,d,2] (iD)

Affiliations are included on p. 11.

Advancing our understanding of brain function and developing treatments for neurological diseases hinge on the ability to modulate neuronal groups in specific brain areas without invasive techniques. Here, we introduce Airy-beam holographic sonogenetics (AhSonogenetics) as an implant-free, cell type–specific, spatially precise, and flexible neuromodulation approach in freely moving mice. AhSonogenetics utilizes wearable ultrasound devices manufactured using 3D-printed Airy-beam holographic metasurfaces. These devices are designed to manipulate neurons genetically engineered to express ultrasound-sensitive ion channels, enabling precise modulation of specific neuronal populations. By dynamically steering the focus of Airy beams through ultrasound frequency tuning, AhSonogenetics is capable of modulating neuronal populations within specific subregions of the striatum. One notable feature of AhSonogenetics is its ability to flexibly stimulate either the left or right striatum in a single mouse. This flexibility is achieved by simply switching the acoustic metasurface in the wearable ultrasound device, eliminating the need for multiple implants or interventions. AhSonogentocs also integrates seamlessly with in vivo calcium recording via fiber photometry, showcasing its compatibility with optical modalities without cross talk. Moreover, AhSonogenetics can generate double foci for bilateral stimulation and alleviate motor deficits in Parkinson's disease mice. This advancement is significant since many neurological disorders, including Parkinson's disease, involve dysfunction in multiple brain regions. By enabling precise and flexible cell type–specific neuromodulation without invasive procedures, AhSonogenetics provides a powerful tool for investigating intact neural circuits and offers promising interventions for neurological disorders.

sonogenetics | focused ultrasound | Airy beam | hologram | neuromodulation

Sonogenetics has emerged as a promising technique for implant-free and cell type–specific neuromodulation (1, 2). Like optogenetics, this technique employs ultrasound to modulate neurons genetically engineered to express ultrasound-sensitive mediators/actuators. Unlike other chemical and physical stimuli used for neuromodulation, ultrasound can noninvasively penetrate the skull and brain, focusing energy within specific regions of animal and human brains (3). Furthermore, ultrasound devices can be designed to manipulate acoustic wave propagation to precisely control ultrasound fields' direction, focus, and shape (4). These characteristics of ultrasound offer the promise for sonogenetics to achieve spatially precise and flexible stimulation throughout the entire brain without the requirement for surgical implants.

Sonogenetics has made significant progress in recent years, evolving from its use in Caenorhabditis elegans to mammalian models, particularly mice. Ibsen et al. first introduced sonogenetics in 2015 (1) using Caenorhabditis elegans, where they artificially overexpressed TRP-4 in specific neurons and induced behavior changes in the presence of microbubbles. This initial approach relied on microbubbles to enhance the mechanical effects of ultrasound on TRP-4, a technique not feasible for mammalian models. Recent advancements have shifted focus to ectopically expressing ultrasound-sensitive mediators in mouse brains without microbubbles. Mediators such as MscL (5–7), Prestin (8, 9), hsTRPA1 (10), and TRPV1 (11, 12) have been utilized. Early feasibility studies in anesthetized mice demonstrated successful modulation of motor circuits (5, 9). The development of wearable ultrasound devices further enabled sonogenetics neuromodulation in freely moving mice (11). The first successful modulation of a deep brain site, the striatum, in freely moving mice was achieved using TRPV1-sonogenetics (11). Sonogenetics was later expanded to modulate other neural circuits, such as the reward and visual circuits, through MscL sonogenetics (6, 7). Additionally, sonogenetics showed potential in improving motor behavior in Parkinson's disease mouse models, achieved through performing

Significance

Sonogenetics holds promise for noninvasive and cell type–specific neuromodulation using ultrasound, yet its potential has been constrained by existing wearable technologies. We present the development of Airy-beam holographic sonogenetics (AhSonogenetics) and demonstrate its significant capabilities. AhSonogenetics offers superior precision in targeting specific subregions of the brain and unparalleled flexibility to dynamically shift focus across different brain regions in freely moving mice. Furthermore, it is compatible with in vivo optical calcium recordings without cross talk. Importantly, AhSonogenetics enables bilateral stimulation for alleviating motor deficits in mice with Parkinson's disease, addressing the challenge of simultaneously targeting dysfunction in multiple brain regions. AhSonogenetics represents a multidisciplinary innovation that advances sonogenetic neuromodulation in terms of precision and flexibility.

[1]Z.H. and Y. Yang contributed equally to this work.

[2]To whom correspondence may be addressed. Email: hongchen@wustl.edu.

repeated unilateral stimulation of neurons expressing Prestin (8) or MscL (6).

Despite these achievements, sonogenetics faces significant limitations with the current wearable ultrasound devices, hindering the full realization of its potential in spatial precision and flexible neuromodulation. The first limitation is the large focal region of these devices, which spans the entire mouse brain in the dorsal-ventral direction. This relative large focus compromises spatial targeting accuracy and may result in off-target confounding effects. Only two types of wearable ultrasound devices have been developed for sonogenetics. One type utilized a 0.9 MHz single-element plane transducer, generating a focal region of approximately 5 mm wide and 25 mm deep (estimated based on the transducer beam profile presented in the publication) (6). The other type, reported by our group, aimed to reduce the focal region size by using a 1.5 MHz concave-shaped ultrasound transducer (11). The focal region size was 1.7 mm wide and 9.6 mm deep, yet it still covered the whole depth of the mouse brain. The second limitation is the lack of flexibility in these devices to adjust target locations within a single mouse brain or to target multiple brain regions simultaneously. Once installed, each device is restricted to stimulating a fixed, singular brain site. An emerging solution to overcome these challenges in sonogenetics is using acoustic metasurfaces, which are wavefront-shaping devices with planar profiles and subwavelength thicknesses (13, 14). Acoustic metasurfaces have the potential to manipulate wavefronts and create complex 3D acoustic fields, thus enabling the development of lightweight, head-mounted ultrasound transducers for flexible ultrasound stimulation in freely moving animals. However, the application of acoustic metasurfaces in medical ultrasound is still in its early stages (15), with no reported studies on their use for sonogenetics.

In this study, we introduce Airy-beam holographic sonogenetics (AhSonogenetics), which utilizes Airy beams and 3D-printed metasurface-based wearable transducer technology for spatially precise and flexible sonogenetics neuromodulation. Airy beams, derived from the Airy function (a solution of the Schrödinger equation and paraxial wave equation), exhibit lateral shifts in the transverse plane along a parabolic self-accelerating trajectory (16). Axisymmetric Airy beams achieve ultrasharp focus owing to abrupt increases in intensity at the focus, which can reach three orders of magnitude greater than the acoustic intensity at the initial source plane (17). While Airy beams have found applications in various fields beyond medical ultrasound (18–21), their use in medical ultrasound has been hindered by the complexity of building devices capable of generating Airy beams. Acoustic metasurfaces have been developed for air-borne Airy beams, including those based on the space coiling-up structure and Helmholtz resonator–like structure (22, 23). However, these are for air-borne sound waves with long wavelengths and often require the manufacturing of subwavelength units with complicated microstructures, which poses challenges to the fabrication for ultrasound since the typical wavelength is on the millimeter scale. Our recent work demonstrated the feasibility of producing underwater ultrasound Airy beams using 3D-printed metasurfaces (24). However, further technological advancements are necessary to harness this concept in designing miniaturized wearable ultrasound transducers for sonogenetics applications.

Here, we present the development of wearable ultrasound devices using Airy-beam holographic metasurface and demonstrate capabilities in neuromodulation enabled by AhSonogenetics. Our numerical simulations and ex vivo calibration confirm their ultrasharp focusing capability. These devices are integrated with genetic engineering, enabling implant-free, cell type–specific, spatially precise, and flexible neuromodulation in freely moving mice. Our work showcases four significant capabilities enabled

by AhSonogenetics. First, AhSonogenetics can target neuronal populations within specific subregions of the striatum in a single mouse. This is achieved by dynamically steering the focus of the Airy beam metasurface along the wave propagation direction via frequency tuning of the driving electrical signal. Achieving such a high degree of precise and flexible perturbation is challenging using established optogenetics that rely on implanted fiber-optic light sources or emerging implant-free optogenetics that utilizes diverging infrared light (25). Similarly, conventional techniques like chemogenetics also face difficulties in achieving this level of spatial specificity. Second, AhSonogenetics offers flexibility in performing unilateral stimulation of either the left or right striatum in a single mouse by simply switching the acoustic metasurface. To achieve this task using optogenetics requires implanting two optical fibers in a single mouse, which is infrequently performed due to the associated risk of brain damage. Third, a distinctive advantage of AhSonogenetics is that ultrasound does not interfere with light, enabling the integration of these two modalities without cross talk. This compatibility is demonstrated by integrating AhSonogenetics with in vivo calcium recording via fiber photometry. Last, we show that the Airy-beam holographic metasurface can generate double foci for bilateral stimulation and improve motor deficits in Parkinson's disease mice. This is significant as many brain diseases, including Parkinson's disease, involve dysfunction in multiple brain regions. Effective treatment often requires neuromodulation at multiple sites, such as bilateral electrode implantation in the basal ganglia circuit to treat Parkinson's disease. Previous sonogenetics studies in Parkinson's disease mouse models were limited to single-site targeting. In summary, AhSonogenetics represents a significant advancement in neuromodulation technology. It enables precise investigation of complex neural circuits in intact brains and offers promising targeted interventions for various neurological diseases, including Parkinson's disease.

Results

Wearable Ultrasound Device Fabrication Using Airy-Beam Holographic Metasurfaces. We designed Airy-beam holographic metasurfaces by calculating the Airy-beam pressure profile on the surface of the metasurface, which was subsequently converted into binary phase values (0 and $\pi/2$) (Fig. 1*A*). The focus location of the ultrasound field generated by the designed metasurfaces in the anterior–posterior (AP) and medial–lateral (ML) direction was determined by (x_0, y_0), which are the coordinates used by the Airy function to define the center of symmetry. The focal depth (z), lateral focal region size along the AP/ML axis, and axial focal region size along the dorsal–ventral (DV) axis were determined by two critical Airy function parameters: r_0 and ω, where r_0 was related to the radial position of the primary Airy ring and ω was the radial scaling factor (*SI Appendix*, Fig. S1). The manipulation of these parameters provided precise control over the location and dimensions of the focal region for a single focus. Furthermore, multifocal points at arbitrary locations were achievable through the superimposing method.

To tailor each Airy-beam metasurface to specific experimental requirements, we designed them individually, considering the intended brain target location and the desired focal region size. The aperture size of the metasurface was kept at 13 mm, imposed to match the maximum width of a mouse's head. The effectiveness of each metasurface design was assessed through numerical simulations using a k-space pseudospectral simulation toolbox (26). These simulations account for skull absorption and scattering, utilizing acoustic parameters derived from CT images of the mouse skull (27).
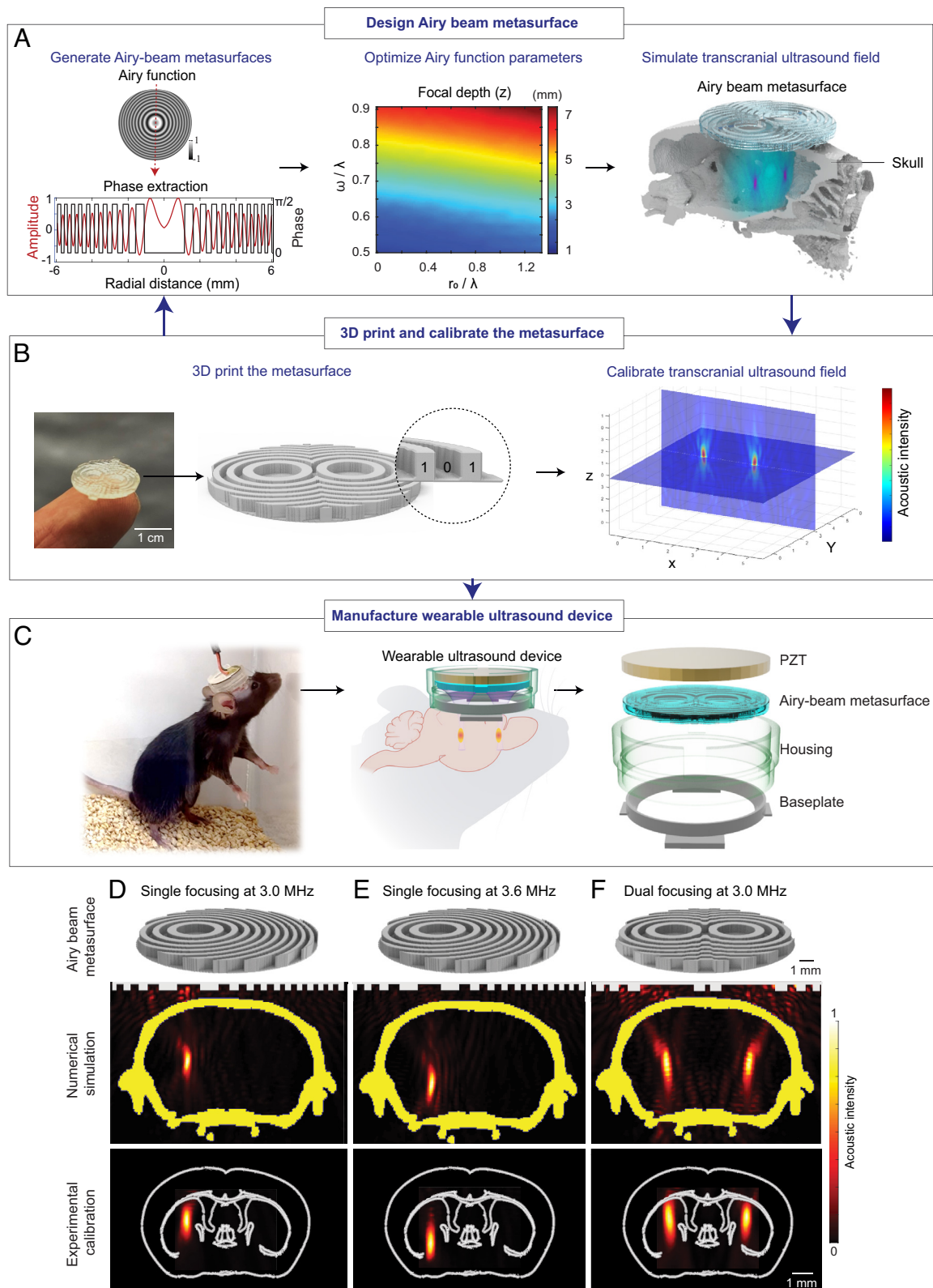
Fig. 1. Wearable ultrasound device design (*A–C*) using Airy-beam holographic metasurfaces and characterization of manufactured device (*D–F*). (*A*) A schematic representation outlining the critical steps involved in Airy-beam metasurface design. The process begins with the initial design by calculating the Airy-beam function amplitude profile, which was converted to binary phase values. This was then followed by optimizing Airy function parameters, including r0 and ω, which are scaled by the wavelength λ, to meet the specific requirements for the intended brain target location and the desired focal region size. The optimized design was then evaluated by numerical simulations of transcranial ultrasound field propagation. (*B*) The designed metasurface is fabricated through 3D printing and calibrated using a hydrophone in a water tank with an ex vivo mouse skull placed in front of the metasurface. (*C*) The wearable ultrasound device is manufactured by integrating the metasurface with a circular-shaped lead zirconate titanate (PZT) ceramic element. A housing was 3D-printed and plugged into a baseplate glued to the mouse head. Three examples are presented to showcase the device's capability in (*D*) off-center beam steering, (*E*) dynamic beam steering along the wave-propagation direction by adjusting the ultrasound frequency without altering the metasurface, and (*F*) dual focusing. In each case, the *Top* panel displays the 3D design of the metasurface, the *Middle* panel presents the numerical simulations of the generated ultrasound fields with the metasurface on the top and yellow highlights denoting the mouse skull, and the *Bottom* panel shows the experimental measurements of the generated ultrasound fields with the white outlines corresponding to brain anatomy in reference to the Allen brain atlas.

Subsequently, the designed metasurfaces were manufactured through 3D printing with two coding bits: a polylactic acid (which is the commonly used 3D printing material) unit acting as a bit "1" and a water unit acting as a bit "0" (Fig. 1B). The height of bit "1" was computed based on the sound speed of polylactic acid to induce a phase shift of $\pi/2$ relative to water. The metasurface's thickness was subwavelength, about 0.8× of the ultrasound wavelength. The 3D-printed metasurfaces were then coupled to a circular-shaped planar lead zirconate titanate (PZT) ceramic element to generate ultrasound. The performance of the metasurfaces was verified through experimental calibrations of the generated ultrasound fields. The calibration was performed using a hydrophone in a water tank with an ex vivo mouse skull placed in front of the metasurface. The metasurface designs were iteratively adjusted until the calibration results aligned with the intended design specifications.

The finalized and validated metasurfaces served as the foundation for the construction of the wearable ultrasound device (Fig. 1C). Each metasurface was integrated with a planar PZT ceramic element and housed within a 3D-printed housing. The housing was plugged into a baseplate. The baseplate was attached to the mouse's head. If needed, this ultrasound device design allows the metasurfaces to be switched to target different brain regions in a single mouse.

Following the pipeline detailed in Fig. 1, we designed and manufactured wearable ultrasound devices for different applications. Fig. 1 D–F illustrates representative Airy-beam holographic metasurfaces. In Fig. 1D, we demonstrate the metasurface's ability to steer the focus off-center to target the left striatum. It achieved sharp focal dimensions of 1.65 mm (axial) × 0.42 mm (lateral) by numerical simulations and 1.73 mm (axial) × 0.46 mm (lateral) by experimental measurements. This focal region size is much smaller than the ~25 mm (axial) × 5 mm (lateral) and 9.6 mm (axial) × 1.7 mm (lateral) achieved by previously reported wearable ultrasound transducers used for sonogenetics (6, 11). Additionally, the focal dimensions of the Airy-Beam transducer are also smaller than those of a single-element concave-shaped transducer for the same brain target. Simulation results for the concave-shaped transducer show focal dimensions of 2.05 mm (axial) × 0.49 mm (lateral) at the same frequency of 3.0 MHz and a focal depth of 6 mm for targeting the same brain location. Notably, the binary design allows continuous steering of the focal point along the wave-propagation direction (the DV axis) by adjusting the operating frequency of the planar transducer (*SI Appendix*, Fig. S2). This feature eliminates the need to replace the metasurface, thus facilitating flexible and dynamic targeting for neuromodulation. This capability is made possible by the altered interaction between the binary acoustic metasurface and the varying wavelength caused by changes in the operating frequency of the acoustic wave (28). Fig. 2E By adjusting the operating frequency of the planar transducer from 3.0 MHz to 3.6 MHz while using the same metasurface as demonstrated in Fig. 1 D and E we can change the focal depth from 4.4 mm to 5.5 mm from the skull without replacing the metasurface. This capability enabled the stimulation of subregions within the striatum in a single mouse without altering the metasurface. In Fig. 1F we present an example of a metasurface designed to generate dual focal points to simultaneously target both sides of the striatum. Our wearable devices, enabled by Airy-beam holographic metasurfaces, offer high precision and flexibility for targeting the mouse brain.

AhSonogenetics for Precise Modulation of Brain Subregions. We subsequently integrated the manufactured wearable ultrasound device with sonogenetics to demonstrate the capability of AhSonogenetics.

Our initial focus was on harnessing dynamic steering for precise sonogenetic modulation of specific subregions of the striatum in a single mouse brain. To demonstrate this capability, we intracranial injected AAV9-CaMKII-TRPV1 into both the dorsal and ventral striatum (Fig. 2A). These particular subregions were chosen based on prior experiments using magnetothermal activation of TRPV1-expressing neurons. In the previous work, magnetothermal genetic activation of TRPV1-expressing neurons in the dorsal striatum elicited rotational movements, while activation of these neurons in the ventral striatum resulted in freezing (29). However, these experiments need to be performed in two different groups of mice, one targeting the dorsal striatum and the other targeting the ventral stratum. Utilizing the Airy-beam metasurface described in Fig. 1 D and E, we sequentially targeted these subregions (Fig. 2A), randomizing the target order in a single mouse. We conducted open-field behavior recordings before, during, and after AhSonogenetic stimulation. Consistent with prior magnetothermal genetic work, AhSonogenetic stimulation of the dorsal striatum specifically evoked rotational behavior toward the contralateral stimulation site with angular velocity increased from -0.04 ± 0.30 rem/min to 0.63 ± 0.15 rem/min during stimulation (Fig. 2B). A control group injected with a control virus (AAV-CaMKII-mCherry) exhibited no changes in either angular or linear speed. In line with our prior findings (11), the ultrasound-targeted region experienced a modest temperature increase of about 1.4 ± 0.1 °C (*SI Appendix*, Fig. S3)., AhSonogenetic stimulation of the ventral striatum led to an average of 37.3% reduction in linear speed, decreasing from 2.68 ± 0.45 mm/s to 1.68 ± 0.26 mm/s, with no accompanying changes in rotational behavior (Fig. 2C). The control group showed no variation in either speed category. The safety of AhSonogenetics stimulation was confirmed through immunohistochemical staining for neurons, astrocytes, and microglia in ex vivo mouse brain slices. The safety assessments were conducted at 1.5 h, 1 d, and 2 d poststimulation (*SI Appendix*, Fig. S4). Collectively, these results underscore the ability of AhSonogenetics to precisely and flexibly target different brain subregions for investigating complex neural functions.

AhSonogenetics for Spatially Flexible Neuromodulation. Next, we performed AhSonogenetics using Airy-beam holographic metasurfaces with a single focus for flexible targeting of either the left or right striatum. We expressed TRPV1 in both the left and right striatum via bilateral injections of AAV-CaMKII-TRPV1 (Fig. 3A). As in our prior experiments, ultrasound unilateral stimulation of the left dorsal striatum in TRPV1+ mice induced clockwise rotational behavior, contralateral to the stimulation site. The angular speed increased from 0.18 ± 0.25 rem/min to 0.94 ± 0.23 rem/min during stimulation. Conversely, when shifting focus to the right striatum, we noted counterclockwise rotational behavior with angular speeds changing from 0.18 ± 0.26 rem/min to -0.52 ± 0.23 rem/min (Fig. 3B). Throughout these unilateral stimulations, linear speeds in TRPV1+ mice remained essentially unchanged (Fig. 3 A and B). Control TRPV1- mice exhibited no significant variations in angular or linear speeds upon ultrasound stimulation.

AhSonogenetics Is Compatible with Existing Optical Neural Recording Technology. We integrated AhSonogenetics with in vivo calcium recording via fiber photometry. We transduced mouse's left and right striatal regions with AAVs to express the calcium reporter, GCaMP6s, and TRPV1. Subsequently, we positioned two fiberoptic cannulas about 200 μm above the injection sites in both regions (Fig. 4A). Two holes, each 2 mm in diameter, were drilled into the Airy-beam holographic metasurface to accommodate the optical fibers (Fig. 4B). Importantly, the
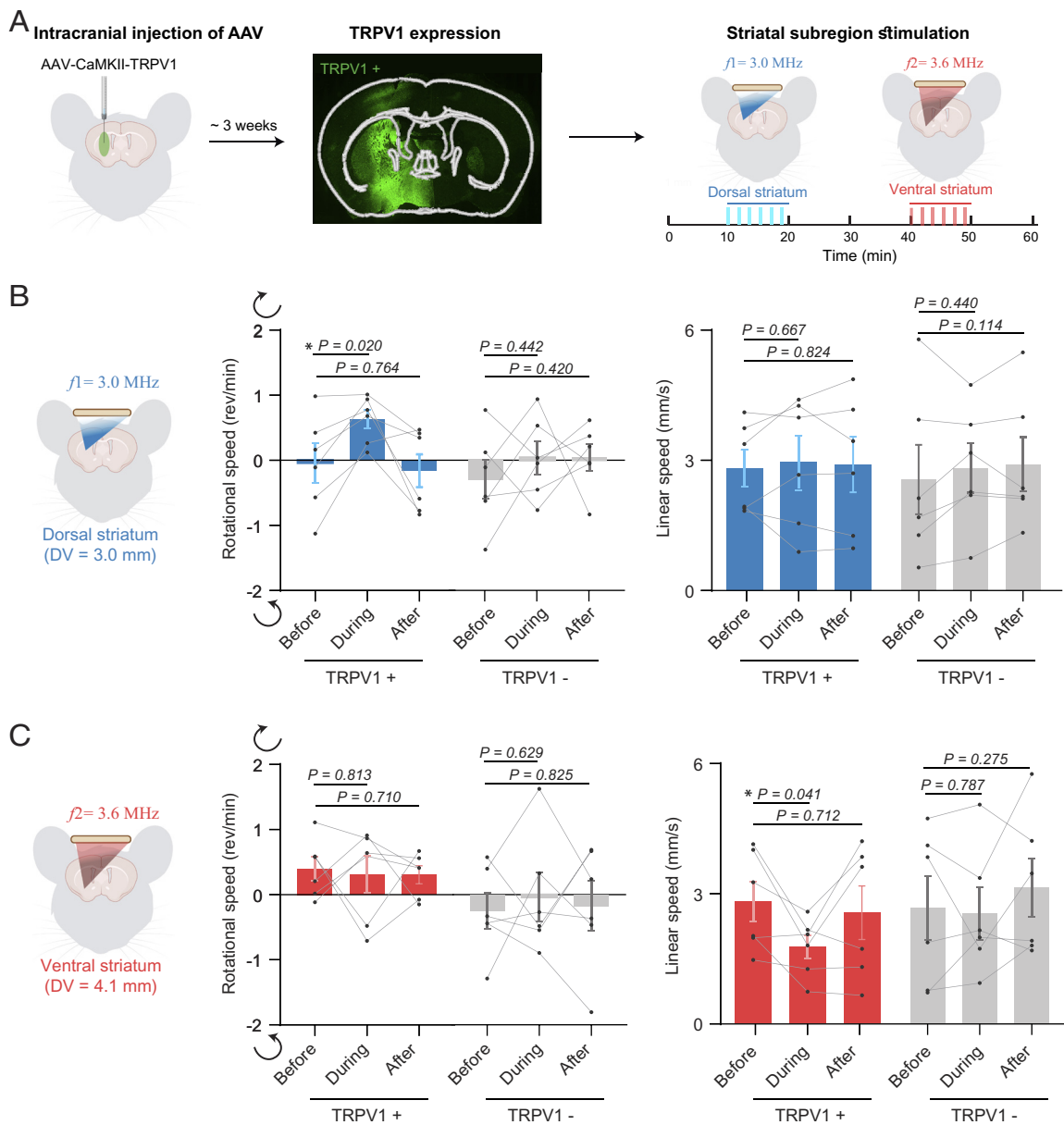
Fig. 2. AhSonogenetics enables precise activation of distinct striatum subregions. (*A*) Schematic illustration of the experimental procedure. AAV-CaMKII-TRPV1 was intracranial injected into the striatum, encompassing dorsal and ventral subregions. Approximately 3 wk after viral injection, TRPV1 expression was validated through immunofluorescence staining using an anti-TRPV1 antibody. The Airy-beam metasurface shown in Fig. 1 *D* and *E* was used to target the dorsal and ventral striatum within a single mouse brain. Every test was composed of six repeated stimuli (shown as blue or red bars). (*B*) Analysis of rotational and linear speeds of TRPV1+ mice (mice injected with AAV9-CaMKII-TRPV1) compared to TRPV1− mice (mice injected with AAV9-CaMKII-mCherry) with ultrasound stimulation at the dorsal striatum. The dorsal–ventral (DV) location of the target was at 3.0 mm. Positive and negative rotational speed values correspond to rotation in the contralateral (clockwise) and ipsilateral (counterclockwise) direction, respectively. (*C*) Analysis of rotational and linear speed of TRPV1+ mice versus TRPV1− mice with ultrasound targeting the ventral striatum (DV = 4.1 mm). The data are based on n = 6 mice in the TRPV1+ and TRPV1− groups. Each mouse received six repeated ultrasound stimulations. Each dot in the bar plot represents the mean of the six repeated measurements for each mouse. Each bar plot represents the mean value across the six mice, with error bars indicating the standard error of mean (SEM). Statistical significance was determined using one-way ANOVA followed by Fisher's LSD multiple-comparison post hoc test.

presence of these holes and the insertion of the optical fibers did not compromise the metasurface's focusing capability (Fig. 4*B*).

When we directed ultrasound to target the left striatum in TRPV1-overexpressing mice, we observed a significant elevation in calcium signaling at the stimulation site (Fig. 4*C*). This was significantly higher than the activity in the contralateral nonstimulated right side. The mean ΔF/F difference between the stimulated (*Left*) and nonstimulated (*Right*) striatum was 0.28 ± 0.08 (Fig. 4*E*). Conversely when we reoriented the ultrasound focus to the right striatum, we noted a corresponding shift in neural activity on the right striatum (Fig. 4*D*). The mean ΔF/F difference was −0.35 ± 0.14 (Fig. 4*F*). Unilateral striatum stimulation not only

elicited a Ca^{2+} response at the target site but also increased activity in the contralateral striatum, although to a lesser degree. While striatal output projections are primarily unilateral, a small percentage impinges on midbrain structures on the contralateral side, allowing control over the contralateral basal ganglia structures (30). Consistent with this anatomy, unilateral optogenetic stimulation of D1R or D2R expressing neurons in the dorsal striatum results in a moderate activation of the contralateral striatum, as observed with functional MRI (31), which is consistent with our observation. Control mice without TRPV1 overexpression exhibited no ultrasound-induced changes in calcium activity. These findings underscore the versatility of AhSonogenetics in
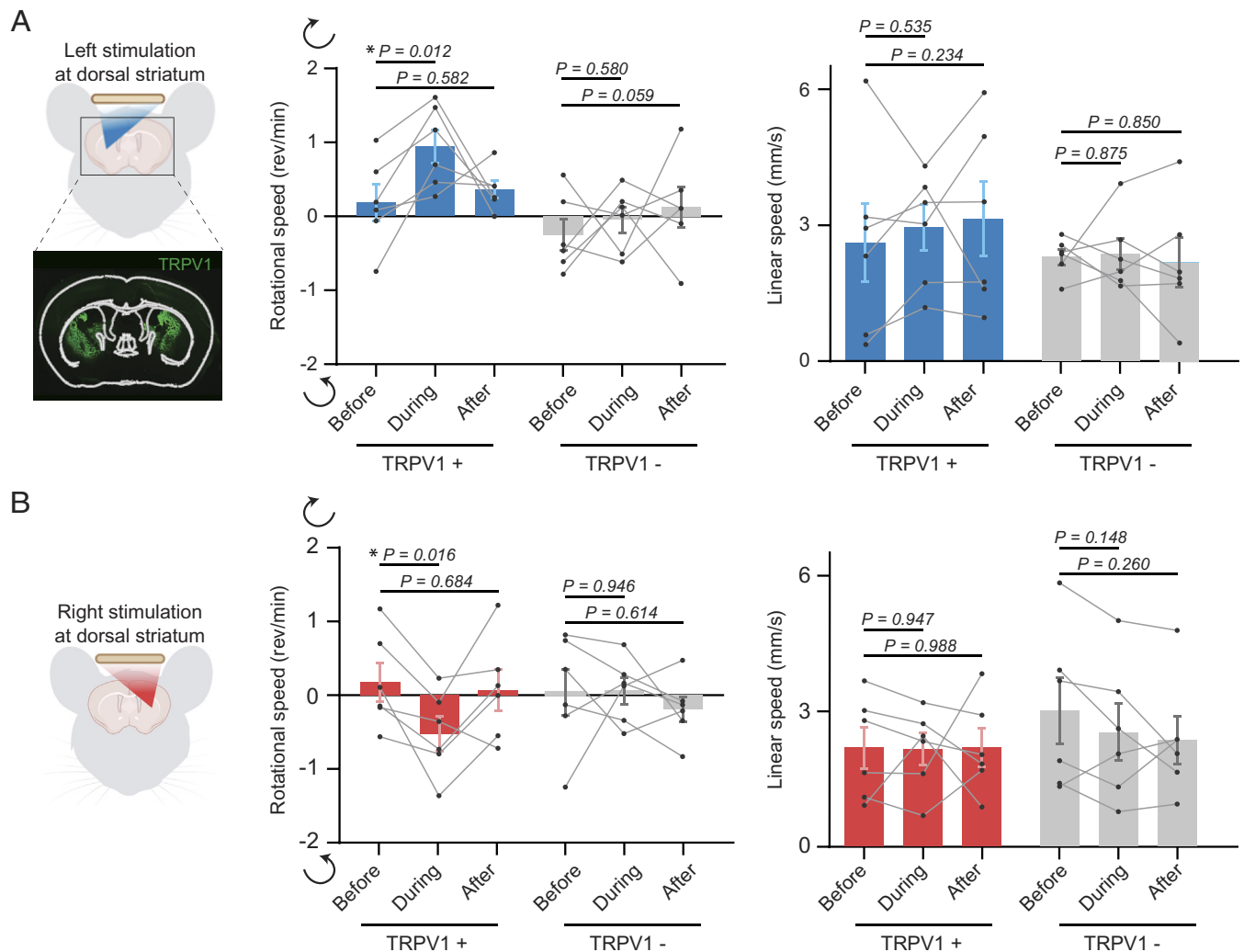
Fig. 3. AhSonogenetics enables spatially flexible neuromodulation. (*A*) AhSonogenetics for unilateral stimulation of the left striatum. (*B*) AhSonogenetics for unilateral stimulation of the right striatum. TRPV1+ mice were engineered to overexpress TRPV1 on both sides of the striatum, and TRPV1− mice were mice injected with control AAVs (AAV-CaMKII-mCherry). The rotational and linear speeds of TRPV1+ and TRPV1− mice before, during, and after-ultrasound stimulation were assessed. The data are based on n = 6 mice in both the TRPV1+ and TRPV1− groups, with each mouse undergoing six repeated stimulations. Each data point in the bar plot represents the mean of the six repeated measurements for each mouse, and each bar represents the mean value among the six mice, with error bars indicating the SEM. Statistical significance was assessed via one-way ANOVA followed by Fisher's LSD multiple-comparison post hoc test.

integrating with brain recording techniques to concurrent monitor (read) and modulate (write) neural activities.

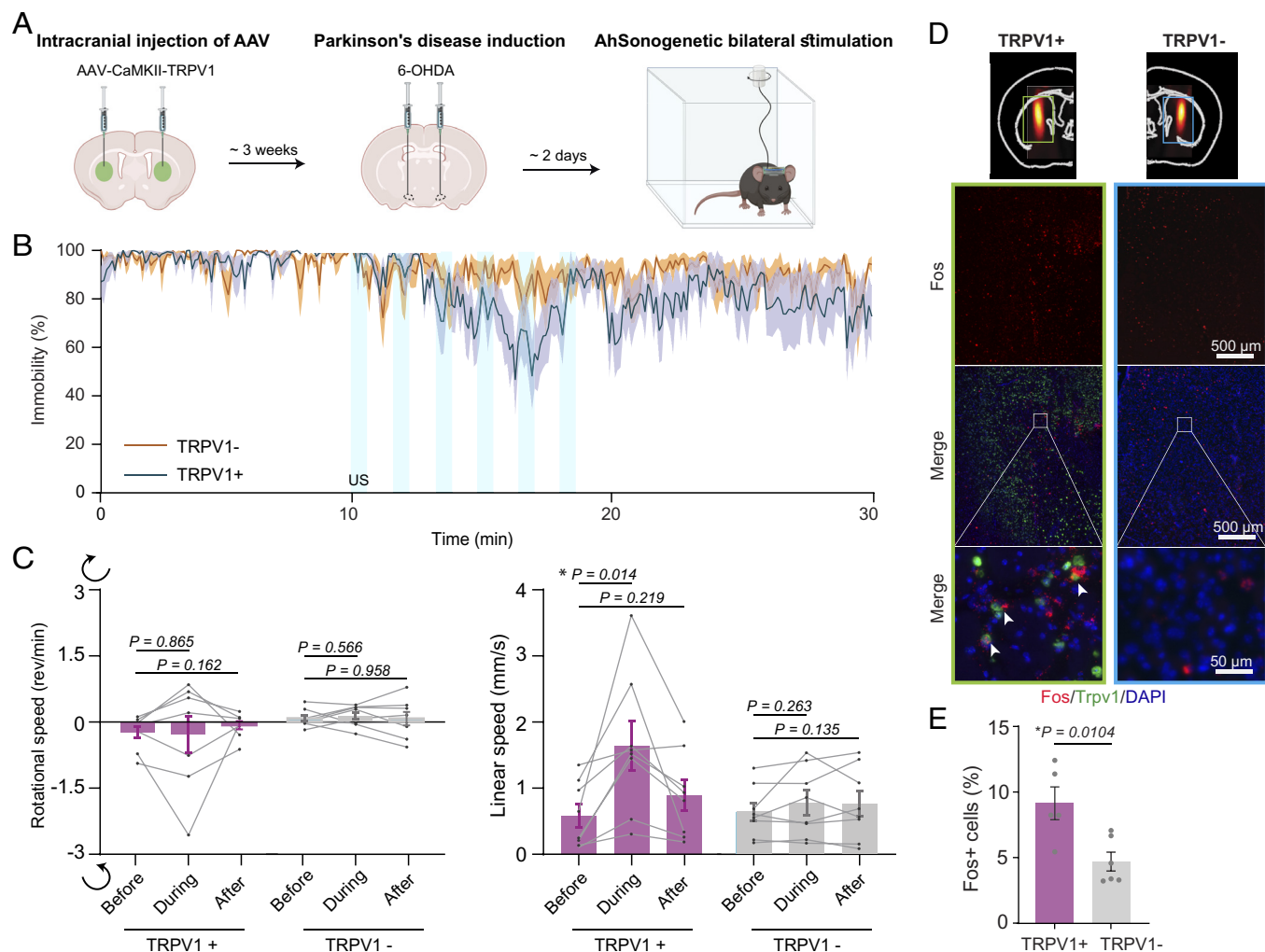**AhSonogenetics Alleviates Motor Deficits in Parkinson's Mice.** Parkinson's disease is primarily characterized by the progressive degeneration of dopaminergic neurons in the substantia nigra, leading to impaired function in the striatal circuits (32). This impairment results in the well-known movement disorders associated with the disease, such as tremors, stiffness, and brady-kinesia. In advanced cases, where pharmacological treatments are less effective or cause significant side effects, neuromodulation therapies, like deep brain stimulation, are often employed (33). These therapies typically involve the bilateral stimulation of specific targets within the basal ganglia circuit to alleviate symptoms. To evaluate the potential of AhSonogenetics in the treatment of Parkinson's disease, we manufactured a metasurface to generate double foci for bilateral targeting of the dorsal striatum (Fig. 1*F*). To establish a Parkinson's disease model in TRPV1+ mice, we initially injected AAVs encoding TRPV1 into the dorsal striatum bilaterally (Fig. 5*A*), followed by 6-OHDA in the medial forebrain bundle to induce dopaminergic neuron depletion (34). The successful creation of dopamine depletion was confirmed by the

ex vivo tyrosine hydroxylase staining in the striatum (*SI Appendix*, Fig. S5). We observed characteristic Parkinsonian motor deficits in the mice, such as bradykinesia, diminished ambulation, hindered locomotor initiation, and increased freezing (35). Modulation of dorsal striatal CaMKII neurons bilaterally via AhSonogenetics using the dual focusing metasurface (Fig. 1*F*) improved the immobility of Parkinson's mice (Fig. 5*B*). Moreover, during the stimulation, the mice exhibited a 2.8-fold increase in linear speed, which rose from 0.61 ± 0.18 mm/s prestimulation to 1.70 ± 1.39 mm/s during stimulation (Fig. 5*C*). Poststimulation, the speed declined to 0.92 ± 0.24 mm/s, a value insignificantly different from that obtained prestimulation. In contrast, the rotational speed remained unaffected by ultrasound stimulation, with values being –0.22 ± 0.14 rem/min prestimulation, –0.27 ± 1.43 rem/min during stimulation, and -0.06 ± 0.10 rem/min poststimulation (Fig. 5*C*). In the control group without TRPV1 overexpression, ultrasound stimulation alone did not significantly alter either linear or angular speed (Fig. 5*C*). AhSonogenetics significantly increased the expression of the neuronal activation marker fos in the targeted striatum by 9.1 ± 1.3%, compared to 4.7 ± 0.7% in the control group (Fig. 5 *D* and E), further demonstrating the activation of neurons by AhSonogenetics in mice with Parkinson's disease.
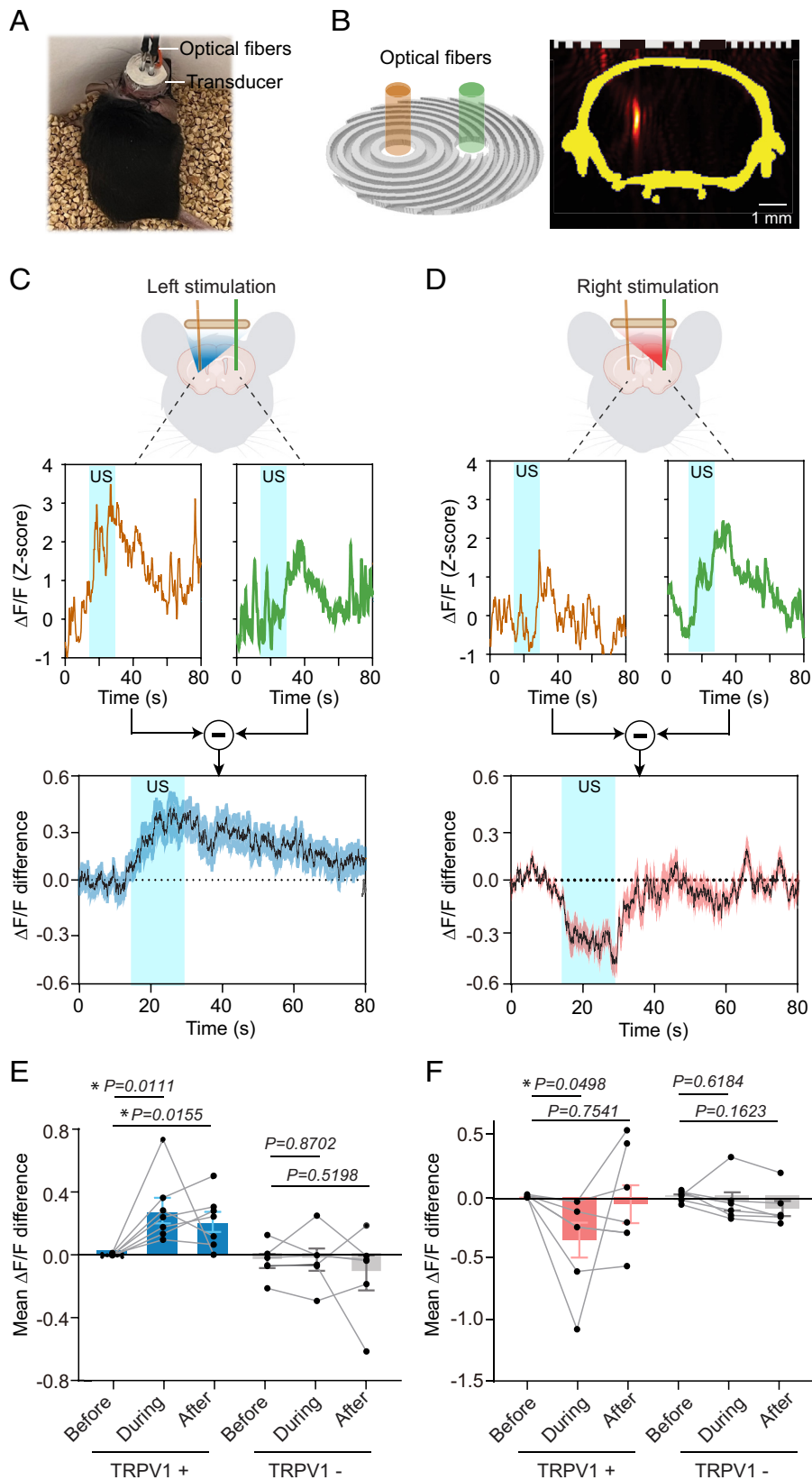
Fig. 4. Integration of AhSonogenetics with fiber photometry. (*A*) Picture of a mouse with a wearable ultrasound device integrated with two optical fibers for fiber photometry recording. (*B*) 3D design of the Airy-beam metasurface for ultrasound stimulation of the left striatum, featuring two holes for optical fiber insertion. Experimental calibration confirmed that the presence of these holes did not compromise the focusing capability of the metasurface. (*C, D*) Representative fiber photometry recording of calcium activities (ΔF/F) in the left and right striatum during ultrasound (US) stimulation at the left (*C*) or right (*D*) striatum. The *Lower* panel presents the calcium activity difference between the left and right striatum with shaded vertical bars indicating the ultrasound stimulation period. (*E* and *F*) Comparison of the mean ΔF/F differences before, during, and after ultrasound stimulation in TRPV1+ mice and TRPV1− mice when ultrasound stimulation in the left (*E*) or right (*F*) striatum. The sample sizes are n = 7 for TRPV1+ mice and n = 6 for TRPV1− mice, with each mouse undergoing six repeated sonications. Each data point in the bar plots represents the mean of the six repeated measurements for each mouse, while each bar plot represents the mean value among all mice and error bars indicate the SEM. The statistical analysis was performed via one-way ANOVA followed by Fisher's LSD multiple-comparison post hoc test.

Fig. 5. AhSonogenetics alleviates motor deficits in a mouse model of Parkinson's disease. (*A*) Schematic illustration of the experimental timeline. (*B*) Assessment of mouse immobility, quantified as the percentage of time spent immobile before, during, and after ultrasound stimulation. The sample size is n = 8 for the TRPV1+ and TRPV1− groups. The solid line represents the mean among measurements from the eight mice, and the shaded area represents the SEM. (*C*) Analysis of rotational and linear speeds in TRPV1+ and TRPV1− mice before, during, and after ultrasound stimulation. The data are based on n = 8 mice in both the TRPV1+ and TRPV1− groups, with each mouse undergoing six repeated stimulations. Each data point in the bar plot represents the mean of the six repeated measurements for each mouse, and each bar represents the mean value among the eight mice. (*D*) Representative images of the spatial distribution of the Fos signal using in situ hybridization method after Airy-beam holographic ultrasound stimulation in TRPV1+ mouse compared to TRPV1− mouse. (*Top*) Fos expression throughout the entire striatum, including the ultrasound target area, corresponding to the rectangular ROI outlined in the mouse brain atlas. (*Middle*) Merged color images combining DAPI (blue), TRPV1 (green), and Fos (red). (*Bottom*) The corresponding zoom-in images. White arrowheads indicate representative fos+ cells. (*E*) Percentage of fos+ cells at ultrasound-targeted striatum in TRPV1+ and TRPV1− groups. n = 5 mice for the TRPV1+ group and n = 6 mice for the TRPV1- group. Error bars indicate the SEM. The statistical analysis was performed via one-way ANOVA followed by Fisher's LSD multiple-comparison post hoc test in panel (*C*) and a two-tailed unpaired Student's *t* test in panel (*E*).

Discussion

AhSonogenetics, integrating Airy-beam holographic metasurface-based wearable ultrasound transducer design with sonogenetics, achieves implant-free, cell type–specific, spatially precise, and flexible neuromodulation. We showcase AhSonogenetics' capability to target striatum subregions, activate neurons unilaterally and bilaterally, and integrate with optical neural recording technology. We also demonstrated its therapeutic potential by alleviating motor deficits in a Parkinson's disease model.

Existing sonogenetics is hindered by spatial imprecision, primarily imposed by the design of conventional ultrasound transducers. AhSonogenetics mitigates these challenges by developing 3D-printed Airy-beam holographic metasurfaces to advance sonogenetics. While our previous work introduced the concept of 3D printed Airy-beam metasurfaces (24), this study marks a breakthrough in developing wearable ultrasound devices using these metasurfaces. These devices were developed by overcoming

challenges with device miniaturization and optimization for precise and flexible brain targeting. AhSonogenetics enables highly accurate perturbation of specific neural circuits, minimizing off-target effects and enhancing our ability to investigate complex neural dynamics. While wearable phased-array ultrasound transducers have been developed for imaging purposes (36–39), they are not ideal for therapeutic applications, which often require a tighter focus and higher energy output than imaging arrays can achieve. Additionally, these phased-array transducers are complex and costly to produce. In contrast, our proposed transducers were fabricated using 3D-printed metasurfaces coupled with a low-cost (~$50) single-element planar transducer. This affordability and ease of fabrication lower the barriers to the widespread adoption of our proposed devices by the research community for neuromodulation applications.

The experiments presented in this study serve as proof-of-concept demonstrations of the capabilities enabled by AhSonogenetics, paving a path toward using this technology as a versatile tool in

neuroscience research. The Airy-beam holographic metasurface can achieve ultrafine spatial focusing, coupled with the flexibility to redirect its focus to arbitrary locations throughout the brain. Moreover, its unique capability to dynamically steer the beam along the axial direction by changing the driving frequency without changing the metasurface offers the flexibility to stimulate different brain regions along the beam axis in a single experiment. While the initial demonstration of AhSonogenetics for multipoint stimulation used bilateral stimulation, the metasurface can generate arbitrary stimulation patterns in 3D, enabling a number of possible stimulation patterns. In addition, optical cross talk between the light sources for optogenetic stimulation and the calcium imaging is a crucial point of consideration for optical experiments. AhSonogenetics can integrate ultrasound stimulation with optical recording to avoid cross talk. In the future, these advancements are expected to expand the scope of current neuromodulation investigations.

Our study underscores the potential of AhSonogenetics as a therapeutic approach to treating neurological diseases. In a Parkinson's mouse mode, we found that AhSonogenetics bilateral stimulation of the dorsal striatum achieved results comparable to those of optogenetics (34), demonstrating similar effectiveness in increasing locomotor velocity. Specifically, AhSonogenetics induced a 2.8-fold increase in locomotor velocity, while optogenetics targeting similar brain regions achieved approximately a 3.6-fold improvement (34). Two previous studies demonstrated the therapeutic benefits of sonogenetics in improving the motor behavior of Parkinson's mice. One study performed 10 min unilateral ultrasound stimulation weekly over 8 wk on Prestin-expressing neurons in mice with Parkinson's disease (8). The other study performed 30 min/d unilateral ultrasound stimulation for 5 consecutive days on MscL-G22S transfected neurons (6). Both studies observed improvements in locomotor behavior following repeated treatment. The former study revealed that the observed beneficial effects were attributed to increased neurotrophin expression following repeated stimulation rather than a direct neuromodulation effect (8). Similar to the previous optogenetic study (34), we performed a single bilateral stimulation and observed the direct neuromodulation effect of sonogenetics in Parkinson's mice, notably without brain implants. This finding establishes a foundation for developing sonogenetics as a neuromodulation treatment for neurological disorders.

AhSonogenetics holds promise for clinical translation, especially considering the existing applications of therapeutic ultrasound in brain disease treatment (3). The Airy-beam holographic metasurface-based wearable ultrasound transducer can be scaled up for human application. Our previous study demonstrated the feasibility of producing an Airy-beam metasurface at a clinically relevant lower frequency of 500 kHz (24) with a large aperture, underscoring its potential for clinical application. A key challenge for clinical use involves the expression of TRPV1 in specific neurons. Recent advancements in blood–brain barrier–permeable AAVs in mice (40) and nonhuman primates (41) present a noninvasive approach for transgene expression. Meanwhile, the use of focused ultrasound in combination with microbubble-mediated blood–brain barrier opening provides another noninvasive approach for delivering intravenously injected AAVs to spatially targeted brain locations in mice (42) and nonhuman primates (43). These emerging noninvasive gene delivery techniques hold the potential for future integration into AhSonogenetics, potentially enabling entirely noninvasive and flexible control of neural activity in the human brain.

This study has several limitations that should be acknowledged. First, once the Airy-beam holographic metasurface is fabricated, its focus location becomes fixed. Achieving dynamic focus at arbitrary positions, except along the axial direction, remains unattainable. While multielement phased arrays offer a potential solution, their complex design and substantial weight of phased arrays have posed significant challenges in developing wearable transducers for mice. Future research is needed to develop innovative strategies for arbitrary dynamic focusing using the Airy-beam holographic metasurface. Second, acoustic holograms designed using the time-reversal approach were used in ultrasound neuromodulation without genetic engineering (44, 45). However, these devices used acoustic lenses with thicknesses much greater than the wavelength; therefore, they tend to be bulky. In contrast, Airy-beam metasurfaces are characterized by their subwavelength-scale design, enabling the design of lightweight wearable transducers. Airy beams offer the unique capability to achieve ultrasharp focusing, which is impossible with the time-reversal acoustic holograms. Nevertheless, future studies are needed to perform side-by-side comparisons to understand the strengths and limitations of all designs. Third, while Airy beams can achieve sharp focus, they are still constrained by their elongated beam pattern. This pattern may inadvertently stimulate adjacent brain regions, especially along the dorsal–ventral axis. Further research is necessary to enhance the focusing ability of focused ultrasound transducers along the dorsal–ventral axis. Last, this study focuses on advancing the ultrasound device design for sonogenetics. However, there is a need for future research to develop advanced ultrasound-sensitive mediators to improve sonogenetics further.

In conclusion, AhSonogenetics represents a critical advancement in neuromodulation technology development, offering a robust solution to many of the limitations inherent in existing methods. Its unique capabilities for implant-free, cell type–specific, spatially precise, and flexible neuromodulation make it a powerful tool for advancing our understanding of complex neural circuits in the intact brain. It also offers significant promise for developing targeted therapies for neurological disorders. As this technology continues to evolve, AhSonogenetics is poised to become an invaluable resource in scientific inquiry and clinical applications.

Materials and Methods

Animals. C57BL/6NCrl mice (female and 6 to 9 wk, Charles River Laboratories) were randomly assigned into different study groups for this study. The mice were housed at the Washington University School of Medicine animal facility, where they were kept in a controlled environment with a temperature of 23 to 26 °C and humidity levels between 35 to 65%. The mice were also given a standard chow diet and subjected to a 12-h light/dark cycle. All animal studies conducted in this research were reviewed and approved by the Institutional Animal Care and Use Committee (IACUC) of Washington University in St. Louis. These studies were carried out in accordance with the NIH Guidelines for Animal Research, and the assigned animal protocol number was 21-0187. Litter and cage mates were randomly divided between experimental groups for all studies. Treatment was performed in a randomized order.

Airy-Beam Holographic Metasurface Design and Manufacturing. The metasurfaces were designed by adapting the concept of producing Airy beams using 3D-printed metasurfaces, as introduced in our prior work (24). Specifically, the Airy beam pressure profile was described by the following equation:

$$p(x,y) = Ai\left(\frac{r_0 - \sqrt{(x-x_0)^2 + (y-y_0)^2}}{\omega} \right) e^{\left(\alpha \frac{r_0 - \sqrt{(x-x_0)^2 + (y-y_0)^2}}{\omega} \right)},$$

Here, $Ai(s)$ denotes the Airy function, r_0 determines the position of the primary Airy ring, ω is the radial scaling factor, and α is the amplitude decay factor. The

coordinates (x, y) represent the coordinates on the initial plane of the metasurface, while (x_0, y_0) defines the focus point position of the Airy-beam metasurface in the xy-plane. The amplitude of the Airy beam at its initial plane was calculated and converted to a binary phase profile. The binary phase profile was then used to design a 3D model of a circular-shaped Airy-beam holographic metasurface with two bits, "1" and "0." The 3D model was printed using a 3D printer (Ultimaker S5, Ultimaker, Netherlands) with polylactic acid plastic as the filament. The polylactic acid represents the bit "1," while water represents the bit "0." The printed Airy-beam holographic metasurface was then coupled with a planar single-element ultrasound transducer with a 13 mm diameter to match the aperture of the printed metasurface.

In our study, we engineered three Airy-beam holographic metasurfaces (46). The first metasurface was for targeting the dorsal left striatum with the intended target location selected to be at anterior–posterior (AP) = 0.0 mm, medial–lateral (ML) = 2.2 mm, and dorsal–ventral (DV) = 3.0 mm (Fig. 1D). The desired axial and lateral focal region size was chosen to be ~1.5 mm and ~0.5 mm, respectively. We chose 1.5 mm as the desired axial focal region size because the mouse striatum is ~3 mm in the AP direction, and we intended to target the dorsal or ventral striatum separately. The lateral focal region size was selected to be 0.5 mm to achieve high spatial resolution in the lateral direction. The metasurface designs were iteratively adjusted until the calibration results aligned with the intended design specifications. The final optimal Airy-beam parameters selected were frequency = 3.0 MHz, $x_0 = 2.2$ mm, $y_0 = 0$ mm, $r_0 = 0.85$, and $\omega = 0.7$. This metasurface was used to stimulate the dorsal striatum and ventral striatum (AP = 0.0 mm, ML = 2.2 mm, DV = 4.1 mm) by utilizing its capability to achieve dynamic ultrasound beam steering along the axial direction by adjusting the ultrasound frequency from 3.0 MHz to 3.6 MH (Fig. 1E). The second metasurface was designed for targeting the dorsal right striatum with the desired ultrasound beam focus located at anterior–posterior (AP) = 0.0 mm, medial–lateral (ML) = −2.2 mm, and dorsal–ventral (DV) = 3.0 mm. The optimal Airy-beam parameters selected were frequency = 3.0 MHz, $x_0 = -2.2$ mm, $y_0 = 0$ mm, $r_0 = 0.85$ and $\omega = 0.7$. The third metasurface was designed to target the dorsal left and right striatum simultaneously by superimposing Airy-beam patterns on each side (Fig. 1F).

Numerical Simulation of Ultrasound Field. 3D numerical simulations were performed to assess the designed Airy beam metasurfaces using the k-space pseudospectral method-based solver, k-Wave (26). These simulations were performed by coupling the metasurface with a flat ultrasound transducer. To accurately represent the acoustic interaction with the skull, we derived the skull's acoustic properties from computed tomography (CT) scans of a mouse head using a μCT scanner (Rigaku). The acquired CT images comprised 512 × 512 × 679 voxels with a spatial resolution of 0.08 mm. A temporal duration of 100 μs was used for all the simulations. The time steps were set as 10 ns for 3.0 MHz and 3.6 MHz to ensure that the Courant–Friedrichs–Lewy (CFL) stability factors used in all the simulations were within 0.3. The density and sound speed of the skull and brain tissue were converted from the Hounsfield units of the CT images using the function "hounsfield2density" in the k-Wave toolbox.

Experimental Calibration of the Wearable Ultrasound Device. The holographic Airy-beam transducer system was developed by integrating an Airy-beam metasurface with a planar transducer (Model DL-47, Del Piezo Specialties). This transducer's piezoelectric material had a central frequency of 3.0 MHz and a bandwidth of 50%, sufficiently broad to encompass all the ultrasound driving frequencies used in our experiments. The acoustic pressure output of the wearable ultrasound device was calibrated with an ex vivo mouse skull placed in front of it to take into the attenuation and scattering effects of the skull. The transducer with the skull was placed in a water tank filled with degassed and deionized water. A hydrophone (HGL-200, ONDA Corporation) was used to map the acoustic fields. The hydrophone was connected to a preamplifier (AH-2010, Onda Corp.) and a digital oscilloscope (Picoscope 5443D, St. Neots, United Kingdom). It was moved in 3D using a computer-controlled 3D stage (PK245-01AA, Velmex Inc.) at a step size of 0.3 mm over a scanning volume covering the ultrasound fields' focal regions. The calibration was conducted by driving the ultrasound transducer with a 20-cycle pulsed wave with a pulse repetition frequency of 100 Hz.

Intracranial Injection of AAVs. All surgeries were performed under aseptic conditions. Mice were anesthetized with 2% isoflurane in oxygen in an anesthetic

chamber for induction and 1.5% isoflurane for maintaining anesthesia. Before the virus injection, buprenorphine (Buprenex, 0.1 μg/g body weight) and carprofen (Rimadyl, 5 μg/g body weight) were injected subcutaneously. Using a bite bar and ear bars, anesthetized mice were then fixed onto a stereotaxic frame (Kopf Instruments). We injected 0.24 μL of either AAV9-CaMKII-TRPV1-p2a-mcherry (4.4 × 10^{13} vg/mL) or AAV9-CaMKII-mcherry (1.2 × 10^{13} vg/mL) into the striatum at a controlled rate of 0.6 μL/min utilizing a microinjector (Nanoject II, Drummond Scientific Company). The stereotaxic coordinates for the dorsal striatum injections were set at anteroposterior (AP) = 0.0 mm, mediolateral (ML) = 2.2 mm, and dorsoventral (DV) = 3.0 mm relative to bregma, with the ventral striatum targeted at DV = 4.1 mm. Both the dorsal and ventral striatum received the same volume of injection, 0.24 μL, for assessing the dynamic steering capabilities of the ultrasound beam. For experiments involving ultrasound beam steering to either the left or right striatum, the virus was bilaterally injected into the dorsal striatum, with each site receiving 0.24 μL. We retracted the needle at approximately 0.5 mm/min postinjection to mitigate tissue disruption. The incision was closed using sutures, and mice were placed on a heating pad to aid recovery. In the postoperative phase, a continuous regimen of anti-inflammatory and antibiotic medications, specifically sulfamethoxazole (1 mg/mL), trimethoprim (0.2 mg/mL), and carprofen (0.1 mg/mL), was provided in the drinking water.

AhSonogenetic Neuromodulation and Behavior Testing. Three weeks after the AAV injection, the baseplate was glued on the mouse skull through the following procedure. We first anesthetized the mouse and stabilized its head in a stereotactic frame. We then marked the bregma as the central point for baseplate alignment (AP = 0.0 mm, ML = 0.0 mm). Next, the baseplate was positioned over the mouse's skull using an insert as a guide. The insert had a hole in the middle. The baseplate position was adjusted to align the hole with the marker on the bregma. Once aligned, we removed the insert and fixed the baseplate with dental cement. After baseplate implantation, mice were given at least 3 d to recover and adapt to the baseplate.

AhSonogenetic neuromodulation commenced at least 3 d after-baseplate installation. We filled the wearable ultrasound device designed for a specific experiment with degassed ultrasound gel and plugged it into the baseplate. Before testing, mice equipped with the device were acclimatized to the behavioral test settings for 2 d (1 h daily). We then administered ultrasound stimulations with the following parameters: 0.85 MPa peak negative pressure, 40% duty cycle, 10 Hz pulse repetition frequency, 15-s stimulus duration, 85-s interval between stimuli, and six repeated stimuli. These parameters were similar to those used in our previous study for evoking locomotor behavior (11). We consistently maintained the peak negative pressure at 0.85 MPa across all experiments by adjusting the PZT element's input signal amplitude according to our hydrophone calibration of the relationship between the input electrical signal and the output acoustic pressure.

Mice's locomotion was recorded using a camera (Logitech C920X, 30 fps) before, during, and after ultrasound stimulation. The recorded videos were analyzed with Bonsai software (v2.7) to determine positional coordinates and angular data. A custom MATLAB script then processed these data to calculate rotational and linear velocities at 15-s intervals before, during, and after each ultrasound stimulus. We then derived the mean rotational and linear speeds across all six stimulations to represent each mouse's locomotor activity. In the Parkinson's disease model study, we also calculated the relative immobility, defined by the percentage of time the linear velocity was below a motion threshold determined by the mean minus twice the SD of the prestimulation periods' linear velocity.

Immunofluorescence Staining. Approximately 1.5 h after AhSonogenetic stimulation, mice were killed by transcardial perfusion with phosphate-buffered saline followed by 4% paraformaldehyde (PFA). Brains were collected, fixed in 4% PFA overnight, and equilibrated in 30% sucrose (in 1× phosphate-buffered saline) for cryosectioning. The fixed brains were sectioned into 15-μm slices for immunohistochemistry staining. Immunohistochemistry staining was performed using the following primary antibodies: anti-NeuN (Abcam, cat. no. 104225, 1:1,000 dilution), anti-GFAP (Abcam, cat. no. 207165, 1:1,000 dilution), anti-Iba1 (Abcam, cat. no. 178846, 1:1,000 dilution), anti-TRPV1 (Invitrogen, cat.no. PA5-77317, 1:500 dilution), and tyrosine hydroxylase (Sigma-Aldrich, cat.no. AB152, 1:500, dilution). FISH staining using the RNA-scope assay was performed following the manufacturer's protocol for RNA-scope Multiplex Fluorescent v2 kit [Advanced

Cell Diagnostics (ACD), 323110]. The RNA-scope probes used were Mm-FOS (ACD, 316921) and Rn-TRPV1 (ACD, 501161). The stained brain slices were imaged using the multichannel Keyence BZ-X800 microscope with a ×20 objective and BZ-X800 Analyzer software (Keyence Corp.). Quantification was conducted utilizing QuPath software (version 0.4.3), with the selection encompassing the entire striatum to ensure the inclusion of the ultrasound-targeted region.

Parkinson's Disease Mouse Model Development. One microliter of 6-OHDA (5 µg/µL in 0.9% NaCl; Sigma-Aldrich) was bilaterally injected into the median forebrain bundle (AP: −0.5 mm, ML: ±1.1 mm, DV: −5 mm) at a rate of 0.3 µL/min following the same procedure described above for AAV injection. Tyrosine hydroxylase immunohistochemistry was performed on ex vivo mouse brain sections to verify dopaminergic neuronal depletion.

Fiber Photometry Recording. To monitor neuronal response induced by AhSonogenetics within the targeted brain regions, we recorded GCaMP signals using fiber photometry. We administered a mixed solution of AAV9-CaMKII-TRPV1-p2A-mcherry (0.24 µL, 4.4×10^{13} vg/mL) and AAV9-CaMKII-GCaMP (0.3 µL, 1.0×10^{13} vg/mL, Addgene) bilaterally into both the left and right striatum. The control group received AAV9-CaMKII-mcherry (0.24 µL, 1.2×10^{13} vg/mL). Following a 3-wk postinjection period, we implanted two fiberoptic cannulas (Doric Lenses Inc.) approximately 200 µm above each injection site. The cannulas were fixed and stabilized with adhesive cement, and the mice were allowed to recover for 1 wk.

A unique Airy-beam metasurface transducer, accommodating two 1.5-mm diameter channels for the fiberoptic cables, was engineered specifically for simultaneous AhSonogenetic stimulation and photometric data capture. These channels enabled precise targeting of the left and right striatum (ML = ±2.2 mm). Extensive simulation and calibration were conducted to quantify the transducer's ultrasound field and pressure output.

In the neuromodulation experiments, the wearable ultrasound device was connected to the baseplate, and optical fibers were connected to the cannulas. A fiber photometry system (FP3002, Neurophotometrics LLC) delivered excitatory blue light (470 nm wavelength, at 4% power) and captured photon emissions from GCaMP6s within both left and right striatum. The system collected and digitized the signals in synchronization with ultrasound applications. We used Bonsai (v.2.7), an open-source platform, for photometry data acquisition and synchronization via an LED signal. We alternated the ultrasound focus between the left and right striatum by swapping the metasurface. The processing of the calcium signal data involved calculating the mean normalized fluorescence changes (ΔF/F) over three distinct periods: 15 s preultrasound, during the 15-s ultrasound application, and the subsequent 45 s following the protocol outlined in ref. 47.

Employing the same transducer design, we assessed the in vivo temperature increase in the ultrasound-targeted brain area using a fiber-optic thermometer (Luxtron, now LumaSense Technologies).

Statistical Analysis. Statistical tests were conducted using GraphPad (Prism). Data were analyzed using one-way ANOVA followed by Fisher's LSD multiple-comparison post hoc test. Statistical differences were considered significant whenever $P < 0.05$. Data are presented as the mean ± SEM in both the figures and the main manuscript, as indicated in the figure legends.

Data, Materials, and Software Availability. We have uploaded the design file for the Airy-beam holographic transducer to GitHub: https://github.com/ChenUltrasoundLabWUSTL/AiryBeam_Lens_Design (46). Additionally, the plasmid is available through Addgene (Plasmid #200829). All other data are included in the manuscript and/or *SI Appendix*.

Author affiliations: ªDepartment of Biomedical Engineering, Washington University in St. Louis, Saint Louis, MO 63130; ᵇDepartment of Psychiatry, Washington University School of Medicine, Saint Louis, MO 63110; ᶜDepartment of Neurosurgery, Washington University School of Medicine, Saint Louis, MO 63110; and ᵈMallinckrodt Institute of Radiology, Washington University School of Medicine, Saint Louis, MO 63110

Author contributions: Z.H., Y. Yang, and H.C. designed research; Z.H., Y. Yang, L.Y., Y.G., C.C., D.Y., Y. Yue, J.Y., A.V.K., and H.C. performed research; Z.H., Y. Yang, L.Y., and H.C. analyzed data; and Z.H., Y. Yang, A.V.K., and H.C. wrote the paper.

1. S. Ibsen, A. Tong, C. Schutt, S. Esener, S. H. Chalasani, Sonogenetics is a non-invasive approach to activating neurons in *Caenorhabditis elegans*. *Nat. Commun.* **6**, 8264 (2015).
2. T. Liu *et al.*, Sonogenetics: Recent advances and future directions. *Brain Stimul.* **15**, 1308–1317 (2022).
3. Y. Meng, K. Hynynen, N. Lipsman, Applications of focused ultrasound in the brain: From thermoablation to drug delivery. *Nat. Rev. Neurol.* **17**, 7–22 (2021).
4. G. Darmani *et al.*, Non-invasive transcranial ultrasound stimulation for neuromodulation. *Clin. Neurophysiol.* **135**, 51–73 (2022).
5. Z. Qiu *et al.*, Targeted neurostimulation in mouse brains with non-invasive ultrasound. *Cell Rep.* **32**, 108033 (2020).
6. Q. Xian *et al.*, Modulation of deep neural circuits with sonogenetics. *Proc. Natl. Acad. Sci. U.S.A.* **120**, e2220575120 (2023).
7. S. Cadoni *et al.*, Ectopic expression of a mechanosensitive channel confers spatiotemporal resolution to ultrasound stimulations of neurons for visual restoration. *Nat. Nanotechnol.* **18**, 667–676 (2023).
8. C. H. Fan *et al.*, Sonogenetic-based neuromodulation for the amelioration of Parkinson's disease. *Nano Lett.* **21**, 5967–5976 (2021).
9. Y. S. Huang *et al.*, Sonogenetic modulation of cellular activities using an engineered auditory-sensing protein. *Nano Lett.* **20**, 1089–1100 (2020).
10. M. Duque *et al.*, Sonogenetic control of mammalian cells using exogenous transient receptor potential A1 channels. *Nat. Commun.* **13**, 600 (2022).
11. Y. Yang *et al.*, Sonothermogenetics for noninvasive and cell-type specific deep brain neuromodulation. *Brain Stimul.* **14**, 790–800 (2021).
12. K. Xu *et al.*, TRPV1-mediated sonogenetic neuromodulation of motor cortex in freely moving mice. *J. Neural. Eng.* **20**, 016055 (2023).
13. B. Assouar *et al.*, Acoustic metasurfaces. *Nat. Rev. Mater.* **3**, 460–472 (2018).
14. S. A. Cummer, J. Christensen, A. Alù, Controlling sound with acoustic metamaterials. *Nat. Rev. Mater* **1**, 16001 (2016).
15. Z. Hu, Y. Yang, L. Xu, Y. Hao, H. Chen, Binary acoustic metasurfaces for dynamic focusing of transcranial ultrasound. *Front Neurosci.* **16**, 1473 (2022).
16. G. A. Siviloglou, J. Broky, A. Dogariu, D. N. Christodoulides, Observation of accelerating Airy beams. *Phys. Rev. Lett.* **99**, 213901 (2007).
17. N. K. Efremidis, D. N. Christodoulides, I. Chremmos, Z. Chen, Abruptly autofocusing waves. *Optics InfoBase Conf. Pap.* **35**, 4045–4047 (2011).
18. N. Voloch-Bloch, Y. Lereah, Y. Lilach, A. Gover, A. Arie, Generation of electron Airy beams. *Nature* **494**, 331–335 (2013).
19. P. Polynkin, M. Kolesik, J. V. Moloney, G. A. Siviloglou, D. N. Christodoulides, Curved plasma channel generation using ultraintense Airy beams. *Science*, 229–232 (2009).
20. J. Baumgartl, M. Mazilu, K. Dholakia, Optically mediated particle clearing using Airy wavepackets. *Nat. Photonics* **2**, 675–678 (2008).
21. T. Vettenburg *et al.*, Light-sheet microscopy using an Airy beam. *Nat. Methods* **11**, 541–544 (2014).
22. Y. Zhang, H. Cheng, J. Tian, S. Chen, Frequency-selected bifunctional coding acoustic metasurfaces. *Phys. Rev. Appl.* **14**, 1 (2020).
23. D.-C. Chen, X.-F. Zhu, D.-J. Wu, X.-J. Liu, Broadband Airy-like beams by coded acoustic metasurfaces. *Appl. Phys. Lett.* **114**, 053504 (2019).
24. Z. Hu, Y. Yang, L. Xu, Y. Jing, H. Chen, Airy-beam-enabled binary acoustic metasurfaces for underwater ultrasound-beam manipulation. *Phys. Rev. Appl.* **18**, 024070 (2022).
25. R. Chen *et al.*, Deep brain optogenetics without intracranial surgery. *Nat. Biotechnol.* **39**, 161–164 (2021).
26. B. E. Treeby, B. T. Cox, k-Wave: MATLAB toolbox for the simulation and reconstruction of photoacoustic wave fields. *J. Biomed. Opt.* **15**, 021314 (2010).
27. Z. Hu, S. Chen, Y. Yang, Y. Gong, H. Chen, An affordable and easy-to-use focused ultrasound device for noninvasive and high precision drug delivery to the mouse brain. *IEEE Trans. Biomed. Eng.* **69**, 2723–2732 (2022).
28. B. Xie *et al.*, Coding acoustic metasurfaces. *Adv. Mater.* **29**, 1603507 (2017).
29. R. Munshi *et al.*, Magnetothermal genetic deep brain stimulation of motor behaviors in awake, freely moving mice. *Elife* **6**, e27069 (2017).
30. C. A. Lieu, T. Subramanian, The interhemispheric connections of the striatum: Implications for Parkinson's disease and drug-induced dyskinesias. *Brain Res. Bull* **87**, 1–9 (2012).
31. H. J. Lee *et al.*, Activation of direct and indirect pathway medium spiny neurons drives distinct brain-wide responses. *Neuron* **91**, 412–424 (2016).
32. B. R. Bloem, M. S. Okun, C. Klein, Parkinson's disease. *Lancet* **397**, 2284–2303 (2021).
33. P. Limousin, T. Foltynie, Long-term outcomes of deep brain stimulation in Parkinson disease. *Nat. Rev. Neurol.* **15**, 234–242 (2019).
34. K. J. Mastro *et al.*, Cell-specific pallidal intervention induces long-lasting motor recovery in dopamine-depleted mice. *Nat. Neurosci.* **20**, 815–823 (2017).
35. A. V. Kravitz *et al.*, Regulation of parkinsonian motor behaviours by optogenetic control of basal ganglia circuitry. *Nature* **466**, 622–626 (2010).
36. H. Hu *et al.*, Stretchable ultrasonic arrays for the three-dimensional mapping of the modulus of deep tissue. *Nat. Biomed. Eng.* **7**, 1321–1334 (2023).
37. M. Lin *et al.*, A fully integrated wearable ultrasound system to monitor deep tissues in moving subjects. *Nat. Biotechnol.* **42**, 448–457 (2024).
38. H. Hu *et al.*, A wearable cardiac ultrasound imager. *Nature* **613**, 667–675 (2023).
39. C. Wang *et al.*, Bioadhesive ultrasound for long-term continuous imaging of diverse organs. *Science* **1979**, 517–523 (2022).
40. K. Y. Chan *et al.*, Engineered AAVs for efficient noninvasive gene delivery to the central and peripheral nervous systems. *Nat. Neurosci.* **20**, 1172–1179 (2017).
41. X. Chen *et al.*, Functional gene delivery to and across brain vasculature of systemic AAVs with endothelial-specific tropism in rodents and broad tropism in primates. *Nat. Commun.* **14**, 1–19 (2023).

42. J. O. Szablowski, A. Lee-Gosselin, B. Lue, D. Malounda, M. G. Shapiro, Acoustically targeted chemogenetics for the non-invasive control of neural circuits. *Nat. Biomed. Eng.* **2**, 475–484 (2018).

43. J. Blesa *et al.*, BBB opening with focused ultrasound in nonhuman primates and Parkinson's disease patients: Targeted AAV vector delivery and PET imaging. *Sci. Adv.* **9**, eadf4888 (2023).

44. G. Kook *et al.*, Multifocal skull-compensated transcranial focused ultrasound system for neuromodulation applications based on acoustic holography. *Microsyst. Nanoeng.* **9**, 45–45 (2023).

45. J. He *et al.*, Simultaneous multi-target ultrasound neuromodulation in freely-moving mice based on a single-element ultrasound transducer. *J. Neural. Eng.* **20**, 016021 (2023).

46. Z. Hu *et al.*, Design files of Airy-beam holographic sonogenetics for advancing neuromodulation precision and flexibility. Github. https://github.com/ChenUltrasoundLabWUSTL/AiryBeam_Lens_Design. Deposited 15 May 2024.

47. T. D. London *et al.*, Coordinated ramping of dorsal striatal pathways preceding food approach and consumption. *J. Neurosci.* **38**, 3547–3558 (2018).